We are IntechOpen, the world's leading publisher of Open Access books Built by scientists, for scientists

4,800
Open access books available

122,000
International authors and editors

135M
Downloads

Our authors are among the

154
Countries delivered to

TOP 1%
most cited scientists

12.2%
Contributors from top 500 universities

WEB OF SCIENCE™

Selection of our books indexed in the Book Citation Index in Web of Science™ Core Collection (BKCI)

Interested in publishing with us?
Contact book.department@intechopen.com

Numbers displayed above are based on latest data collected.
For more information visit www.intechopen.com

21

Spatio-Temporal Measurement of Convective Heat Transfer Using Infrared Thermography

Hajime Nakamura
National Defense Academy
Japan

1. Introduction

Convective heat transfer is, by nature, generally nonuniform and unsteady, a fact reflected by three-dimensional flow near a wall. However, most experimental studies concerning convective heat transfer have been performed in a time-averaged manner or using one-point measurements. This frequently results in poor understanding of the heat transfer mechanisms.
Measurement techniques for the temporal and spatial characteristics of heat transfer have been developed using liquid crystals (Iritani, et al., 1983; among others) or using infrared thermography (Hetsroni & Rozenblit, 1994; among others), by employing a thin test surface having a low heat capacity. However, the major problem with these measurements is attenuation and phase delay of the temperature fluctuation due to thermal inertia of the test surface. This becomes serious for higher fluctuating frequencies, for which the fluctuation amplitude weakens and ultimately becomes indistinguishable from noise. In addition, lateral conduction through the test surface attenuates the amplitude of the spatial temperature distribution. This becomes serious for smaller wavelength (higher wavenumber). These attenuations are considerably large, especially for the heat transfer to gaseous fluid such as air for which the heat transfer coefficient is low.
The recent improvement of infrared thermograph with respect to temporal, spatial and temperature resolutions enable us to investigate detailed behavior of the heat transfer caused by flow turbulence. Analytical study indicated that the spatio-temporal distribution of the heat transfer to air caused by flow turbulence can be observed by employing modern infrared thermograph (for example, NETD less than 0.025 K and frame rate more than several hundred Hz) that records temperature fluctuations on a heated thin foil of sufficiently low heat capacity. In the former part of this chapter (sections 2 – 4), an analytical investigation was described on the frequency response and the spatial resolution of a thin foil for the heat transfer measurements. In order to derive general relationships, non-dimensional variables of fluctuating frequency and spatial wavenumber were introduced to formulate the amplitude of temperature fluctuation and/or distribution on the test surface. Based on these relationships, the upper limits on the detectable fluctuating frequency f_{max} and spatial wavenumber k_{max} were formulated using governing parameters of the measurement system, i.e., thermophysical properties of the thin foil and noise-equivalent temperature difference (NETD) of infrared thermograph for a blackbody.
In the latter part of this chapter, this technique was applied to measure the spatio-temporal distribution of turbulent heat transfer to air by employing a high-speed infrared

thermograph and a heated thin-foil. At first, as a well-investigated case, the heat transfer on the wall of a turbulent boundary layer was measured in order to verify the applicability of this technique (section 5). Also, this technique was applied to explore the spatio-temporal characteristics of the heat transfer behind a backward-facing step, which represents the separated and reattaching flow (section 6).

Nomenclature

b, b_c : spatial wavelength, cut-off wavelength [m]
b_{min} : lower limit of spatial wavelength detectable [m]
c : specific heat [J/kg K]
f, f_c : fluctuating frequency, cut-off frequency [Hz]
f_{max} : upper limit of fluctuating frequency detectable [Hz]
H : step height [m]
h : heat transfer coefficient [W/m^{2}K]
h_t : total heat transfer coefficient including conduction and radiation [W/m^{2}K]
k : wavenumber = $2\pi/b$ [m^{-1}]
l_τ : wall-friction length = ν/u_τ
l_z : mean spanwise wavelength [m]
Nu : Nusselt number; $Nu_H = \bar{h}H / \lambda$
$\dot{q}$: heat flux [W/m^2]
Re : Reynolds number; $Re_H = u_0 H/\nu$, $Re_\theta = u_0\delta_\theta/\nu$
St : Strouhal number $= f H/u_0$
T : temperature [K]
T_0, T_w : freestream temperature, wall temperature [K]
ΔT_{IR} : noise-equivalent temperature difference of infrared thermography for a non-blackbody [K]
ΔT_{IR0} : noise-equivalent temperature difference of infrared thermography for a blackbody [K]
t : time [s]
u_0, u_τ : freestream velocity, wall-friction velocity[m/s]
x, y, z : tangential, normal and spanwise coordinates
α : thermal diffusivity = $\lambda/c\rho$ [m^2/s]
β : space resolution [m]
δ, δ_a : thickness, air-layer thickness [m]
δ_θ : momentum thickness [m]
ε_t : total emissivity
ε_{IR} : spectral emissivity for infrared thermograph
κ : $= \sqrt{\omega / 2\alpha}$ [m^{-1}]
λ : thermal conductivity [W/m·K]
ν : kinematic viscosity [m^2/s]
ρ : density [kg/m^3]
τ : time constant [s]
ω : angular frequency = $2\pi f$ [rad/s]

Subscripts

a, c, i : air layer, high-conductivity plate, insulating layer

cd, *cv* : conduction, convection
rd, *rdi* : radiation to outside, radiation to inside
f, *s* : frequency response, space resolution

Other Symbols

$(\bar{\ })$: mean value
$\Delta(\ ), (\ )_{rms}$: spatial or temporal amplitude, root-mean-square value

2. Analytical solutions without heat losses

2.1 Governing equations

Figure 1 shows a schematic model for heat transfer measurement. The test surface, which is exposed to air flow, is fabricated from a thin metallic foil (thickness δ, specific heat c, density ρ, thermal conductivity λ, and total emissivity ε_t). An instantaneous temperature distribution and its fluctuation on the test surface can be measured using infrared thermography through the air-stream, which is transparent for infrared radiation. Inside the foil, there is a high-conductivity plate (total emissivity ε_{tc}) to impose a thermal boundary condition of a steady and uniform temperature. Between the foil and the high-conductivity plate is some material of low conductivity and low heat capacity, such as still air, forming an insulating layer (thickness δ_i, specific heat c_i, density ρ_i, thermal conductivity λ_i).

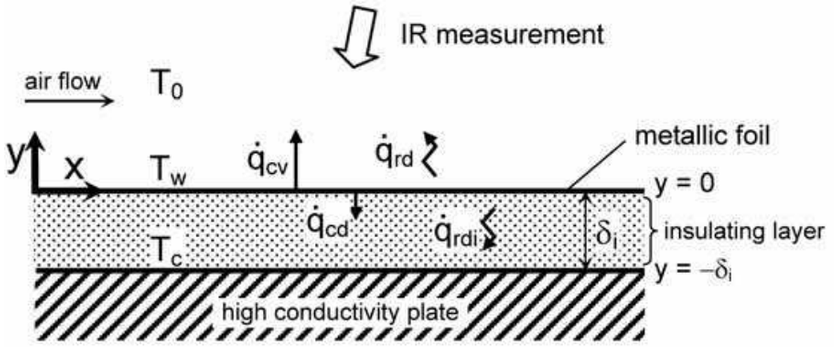

Fig. 1. Schematic model for measurement of heat transfer to air

The tangential and normal directions with respect to the test surface correspond to x and y coordinates, respectively. Assuming that the temperature is uniform along its thickness, the heat balance on the thin foil can be expressed as:

$$c\rho\delta\frac{\partial T_w}{\partial t} = \lambda\delta\left(\frac{\partial^2 T_w}{\partial x^2} + \frac{\partial^2 T_w}{\partial z^2}\right) + \dot{q}\ , (y = 0). \tag{1}$$

Here, T_w is local and instantaneous temperature of the thin foil. The heat flux, $\dot{q}$, is given by:

$$\dot{q} = \dot{q}_{in} - \dot{q}_{cv} - \dot{q}_{cd} - \dot{q}_{rd} - \dot{q}_{rdi} \tag{2}$$

where $\dot{q}_{in}$ is the input heat-flux to the thin foil due to Joule heating, $\dot{q}_{cv}$ and $\dot{q}_{cd}$ are heat fluxes from the thin foil due to convection and conduction, respectively, and $\dot{q}_{rd}$ is radiation heat flux to outside the foil. If the insulating layer is transparent for infrared radiation, as is air, radiation heat flux $\dot{q}_{rdi}$ occurs to the inside. The above heat fluxes are expressed as follows:

$$\dot{q}_{cv} = h\,(T_w - T_0) \tag{3}$$

$$\dot{q}_{cd} = \lambda_i \left(\frac{\partial T}{\partial y} \right)_{y=0-} \tag{4}$$

$$\dot{q}_{rd} = \varepsilon_t\, \sigma({T_w}^4 - {T_0}^4) \tag{5}$$

$$\dot{q}_{rdi} = \frac{\sigma({T_w}^4 - {T_c}^4)}{1/\varepsilon_t + 1/\varepsilon_{tc} - 1} \tag{6}$$

Here, h is the heat transfer coefficient due to convection to the stream outside, T_0 is the freestream temperature, T_c is surface temperature of the high-conductivity plate, and σ is the Stefan-Boltzmann constant.
Heat conduction in the insulating layer is expressed as:

$$c_i \rho_i \frac{\partial T}{\partial t} = \lambda_i \left(\frac{\partial^2 T}{\partial x^2} + \frac{\partial^2 T}{\partial y^2} + \frac{\partial^2 T}{\partial z^2} \right), \; (-\delta_i < y < 0). \tag{7}$$

The frequency response and the spatial resolution of T_w for the heat transfer to the free stream can be calculated using Eq. (1) – (7) for arbitrary changes in the heat transfer coefficient in time and space.

2.2 Time constant

Assuming that the temperature is uniform in the x–z plane, and that heat conduction $\dot{q}_{cd}$ and radiation $\dot{q}_{rd}$ and $\dot{q}_{rdi}$ are sufficiently small, Eq. (1) – (3) yield the following differential equation:

$$c\rho\delta \frac{\partial T_w}{\partial t} = \dot{q}_{in} - h(T_w - T_0)\,. \tag{8}$$

Solving Eq. (8) yields the time constant τ, which is expressed as:

$$\tau = \frac{c\rho\delta}{h}\,. \tag{9}$$

2.3 Spatial resolution

Assuming that the temperature on the test surface is steady and has a sinusoidal distribution in the x direction (uniform in the z direction), then:

$$T_w = \overline{T_w} + \Delta T_w \sin\left(\frac{2\pi}{b} x \right). \tag{10}$$

where $\overline{T_w}$ and ΔT_w are the mean and spatial amplitude of the temperature of the thin foil, respectively, and b is the wavelength. If $\dot{q}_{cd}$, $\dot{q}_{rd}$ and $\dot{q}_{rdi}$ are sufficiently small, Eq. (1) – (3) yield the following equation:

$$h\,(T_w - T_0) = \dot{q}_{cv} = \dot{q}_{in} + \lambda\delta\,\frac{d^2 T_w}{dx^2} \tag{11}$$

If the thin foil is thermally insulated, Eq. (11) reduces to:

$$h\,(T_{w0} - T_0) = \dot{q}_{cv} = \dot{q}_{in}\,. \tag{12}$$

Then, the temperature of the insulated surface T_{w0} is calculated from Eq. (10) – (12) as

$$T_{w0} = \overline{T_w} + \left\{ \frac{\lambda\delta}{h}\left(\frac{2\pi}{b}\right)^2 + 1 \right\} \Delta T_w \sin\left(\frac{2\pi}{b}x\right). \tag{13}$$

A comparison between Eq. (10) and (13) yields the attenuation rate of the spatial amplitude due to lateral conduction through the thin foil:

$$\xi = \frac{1}{\dfrac{\lambda\delta}{h}\left(\dfrac{2\pi}{b}\right)^2 + 1}\,. \tag{14}$$

A spatial resolution β can be defined as the wavelength b at which the attenuation rate is 1/2:

$$\beta = b_{(\xi=1/2)} = 2\pi\sqrt{\frac{\lambda\delta}{h}}\,. \tag{15}$$

Incidentally, if the test surface has a two-dimensional temperature distribution such as:

$$T_w = \overline{T_w} + \Delta T_w \sin\left(\frac{2\pi}{b}x\right)\sin\left(\frac{2\pi}{b}z\right). \tag{16}$$

then the spatial resolution can be calculated as:

$$\beta_{2D} = 2\pi\sqrt{\frac{2\lambda\delta}{h}}\,. \tag{17}$$

This indicates that the spatial resolution for the 2D temperature distribution deteriorates by a factor of $\sqrt{2}$.

3. General relations considering heat losses

In this section, general relationship was derived concerning the temporal and spatial attenuations of temperature on the thin foil considering the heat losses. Since the full derivation is rather complicated (Nakamura, 2009), a brief description was made below.

3.1 Temporal attenuation

Assuming that the temperature on the thin foil is uniform and fluctuates sinusoidally in time:

$$T_w = \overline{T_w} + \Delta T_w \sin(\omega t)\,. \tag{18}$$

Figure 2 shows the analytical solutions of the instantaneous temperature distribution in the insulating layer ($0 \le |y| \le \delta_i$) at $\omega t = \pi/2$, at which the temperature of the thin foil ($y = 0$) is

maximum. The shape of the distribution depends only on $\kappa_i\delta_i$, where $\kappa_i = \sqrt{\omega/(2\alpha_i)}$, α_i is thermal diffusivity of the insulating layer. For lower frequencies ($\kappa_i\delta_i < 1$), the distribution can be assumed linear, while for higher frequencies ($\kappa_i\delta_i >> 1$), the temperature fluctuates only in the vicinity of the foil ($|y|/\delta_i \le 1/\kappa_i\delta_i$).

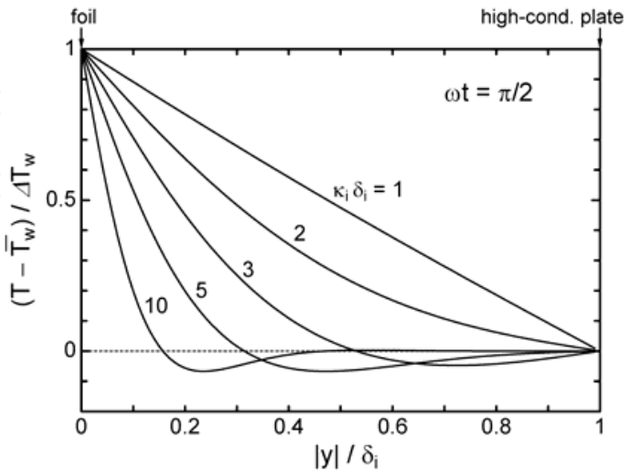

Fig. 2. Instantaneous temperature distribution in the insulating layer at ωt = π/2 and $\overline{T_w} = \overline{T_c}$

Introduce the effective thickness of the insulating layer, $(\delta_i^*)_f$, the temperature of which fluctuates with the thin foil:

$$(\delta_i^*)_f \approx 0.5\delta_i \quad , (\kappa_i\delta_i < 1) \tag{19}$$

$$(\delta_i^*)_f \approx 0.5/\kappa_i \quad , (\kappa_i\delta_i >> 1). \tag{20}$$

The heat capacity of this region works as an additional heat capacity that deteriorates the frequency response. Thus, the effective time constant considering the heat losses can be defined as:

$$\tau^* \approx \frac{c\rho\delta + c_i\rho_i(\delta_i^*)_f}{h_t} \quad , \quad h_t = \frac{\dot{q}_{in}}{T_w - T_0}. \tag{21}$$

Here, h_t is total heat transfer coefficient from the thin foil, including the effects of conduction and radiation. Then, the cut-off frequency is defined as follows:

$$f_c^* = \frac{1}{2\pi\tau^*}. \tag{22}$$

We introduce the following non-dimensional frequency and non-dimensional amplitude of the temperature fluctuation:

$$\tilde{f} = f/\overline{f_c^*} \tag{23}$$

$$(\Delta\tilde{T}_w)_f = \frac{(\Delta T_w)_f}{\overline{T_w} - T_0}\frac{\overline{h_t}}{\Delta h}. \tag{24}$$

Here, $(\Delta\tilde{T}_w)_f$ includes the factor $\overline{h_t}/\Delta h$ to extend the value of $(\Delta\tilde{T}_w)_f$ to unity at the lower frequency in the absence of conductive or radiative heat losses (see Fig. 3).

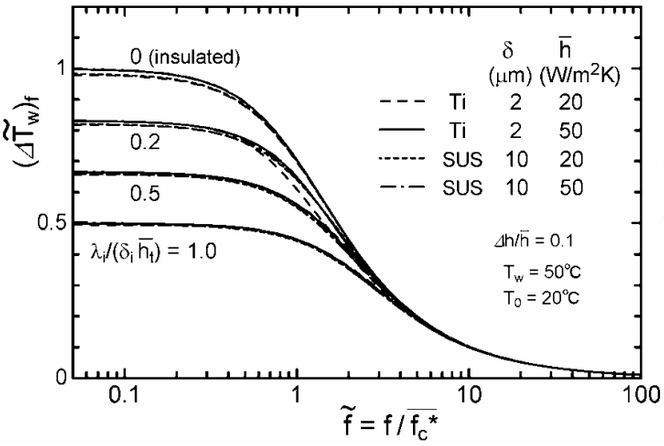

Fig. 3. Relation between non-dimensional frequency $\tilde{f}$ and non-dimensional fluctuating amplitude $(\Delta\tilde{T}_w)_f$

Next, we attempt to obtain the relation between $\tilde{f}$ and $\left(\Delta\tilde{T}_w\right)_f$. The fluctuating amplitude of the surface temperature, $(\Delta T_w)_f$, can be determined by solving the heat conduction equations of Eq. (1) and (7) by the finite difference method assuming a uniform temperature in the x–z plane. Figure 3 plots the relation of $(\Delta\tilde{T}_w)_f$ versus $\tilde{f}$ for practical conditions (see sections 5 and 6). The thin foil is a titanium foil 2 μm thick ($c\rho\delta$ = 4.7 J/m²K, $\lambda\delta$ = 32 μW/K, ε_{IR} = 0.2) or a stainless-steel foil 10 μm thick ($c\rho\delta$ = 40 J/m²K, $\lambda\delta$ = 160 μW/K, ε_{IR} = 0.15), the insulating layer is a still air layer without convection, and the mean heat transfer coefficient is $\overline{h}$ = 20 – 50 W/m²K. A parameter of $\lambda_i/(\delta_i\overline{h_t})$, which represents the the heat conduction loss from the foil to the high-conductivity plate through the insulating layer, is varied from 0 to 1.

For the lower frequency of $\tilde{f}$ < 0.1, $(\Delta\tilde{T}_w)_f$ approaches a constant value:

$$(\Delta\tilde{T}_w)_f \approx \frac{1}{1+\lambda_i/(\delta_i\overline{h_t})}\ ,\ (\tilde{f}<0.1). \tag{25}$$

In this case, the fluctuating amplitude decreases with increasing $\lambda_i/(\delta_i\overline{h_t})$. With increasing $\tilde{f}$, the value of $(\Delta\tilde{T}_w)_f$ decreases due to the thermal inertia. For higher frequency values of $\tilde{f}$ > 4, $(\Delta\tilde{T}_w)_f$ depends only on $\tilde{f}$. Consequently, it simplifies to a single relation:

$$(\Delta\tilde{T}_w)_f \approx \frac{1}{\tilde{f}}\ ,\ (\tilde{f}>4). \tag{26}$$

3.2 Spatial attenuation

Assuming that the temperature on the foil is steady and has a sinusoidal temperature distribution in the x direction (1D distribution):

$$T_w = \overline{T_w} + \Delta T_w \sin(kx)\ ,\ k = 2\pi/b. \tag{27}$$

Here, k is wavenumber of the spatial distribution.

Figure 4 shows the analytical solutions of the vertical temperature distribution in the insulating layer ($0 \le |y| \le \delta_i$) at $kx = \pi/2$, at which the temperature of the thin foil ($y = 0$) is maximum. The shape of the distribution depends only on $k\delta_i$. For the lower wavenumber ($k\delta_i < 1$), the distribution can be assumed linear, while for the higher wavenumber ($k\delta_i >> 1$), the distribution approaches an exponential function.

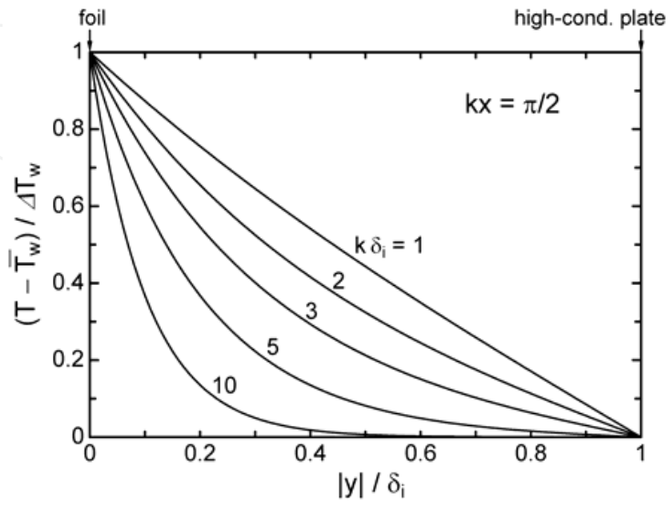

Fig. 4. Temperature distribution in the insulating layer at $kx = \pi/2$ and $\overline{T_w} = \overline{T_c}$

Now, we introduce an effective thickness of the insulating layer, $(\delta_i^*)_s$, the temperature of which is affected by the temperature distribution on the foil:

$$(\delta_i^*)_s \approx \delta_i \ , \ (k\delta_i < 1) \tag{28}$$

$$(\delta_i^*)_s \approx 1/k \ , \ (k\delta_i >> 1) \tag{29}$$

The heat conduction of this region functions as an additional heat spreading parameter that reduces the spatial resolution. Thus, the effective spatial resolution can be defined as:

$$\beta^* \approx 2\pi\sqrt{\frac{\lambda\delta + \lambda_i(\delta_i^*)_s}{h_t}} \ . \tag{30}$$

Introduce a non-dimensional wavenumber and non-dimensional amplitude of the spatial temperature distribution:

$$\tilde{k} = \frac{k}{(2\pi/\overline{\beta^*})} = \frac{k\overline{\beta^*}}{2\pi} \tag{31}$$

$$(\Delta\tilde{T}_w)_s = \frac{(\Delta T_w)_s}{\overline{T_w} - T_0}\frac{\overline{h_t}}{\Delta h} \ . \tag{32}$$

Here, $2\pi/\overline{\beta^*}$ corresponds to the cut-off wavenumber.
Next, we attempt to obtain a relation between $\tilde{k}$ and $(\Delta\tilde{T}_w)_s$. The spatial amplitude of the surface temperature, $(\Delta T_w)_s$, can be determined by solving a steady-state solution of the heat

conduction equations of Eq. (1) and (7) by the finite difference method. Figure 5 plots the relation of $(\Delta\tilde{T}_w)_s$ versus $\tilde{k}$ for practical conditions. For the lower wavenumber of $\tilde{k} < 0.1$, $(\Delta\tilde{T}_w)_s$ approaches a constant value of

$$(\Delta\tilde{T}_w)_s \approx \frac{1}{1+\lambda_i/(\delta_i\overline{h_t})} \ , \ (\tilde{k} < 0.1). \tag{33}$$

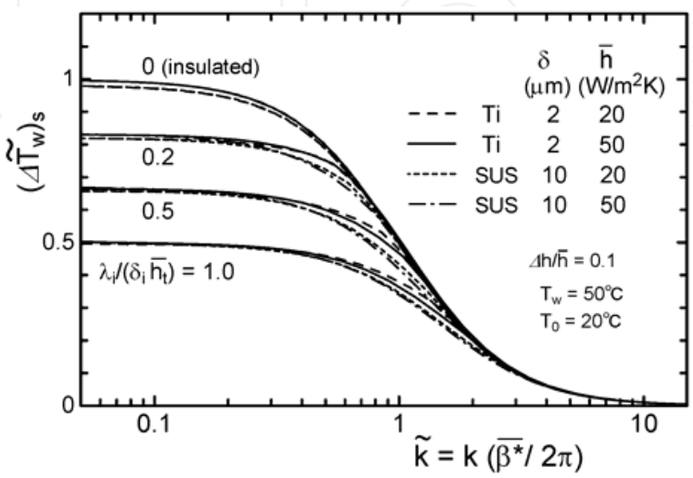

Fig. 5. Relation between non-dimensional wavenumber $\tilde{k}$ and non-dimensional spatial amplitude $(\Delta\tilde{T}_w)_f$

In this case, the spatial amplitude decreases with increasing $\lambda_i/(\delta_i\overline{h_t})$, which represents the vertical conduction. With increasing $\tilde{k}$, the value of $(\Delta\tilde{T}_w)_s$ decreases due to the lateral conduction. For the higher wavenumber of $\tilde{k} > 4$, $(\Delta\tilde{T}_w)_s$ depends only on $\tilde{k}$. It, therefore, corresponds to a single relation.

$$(\Delta\tilde{T}_w)_s \approx \frac{1}{(\tilde{k})^2} \ , \ (\tilde{k} > 4). \tag{34}$$

4. Detectable limits for infrared thermography

4.1 Temperature resolution

The present measurement is feasible if the amplitude of the temperature fluctuation, $(\Delta T_w)_f$, and the amplitude of the spatial temperature distribution, $(\Delta T_w)_s$, is greater than the temperature resolution of infrared measurement, ΔT_{IR}. In general, the temperature resolution of a product is specified as a value of noise-equivalent temperature difference (NETD) for a blackbody, ΔT_{IR0}.

The spectral emissive power detected by infrared thermograph, E_{IR}, can be assumed as follows:

$$E_{IR}(T) = \varepsilon_{IR} C T^n \ . \tag{35}$$

where ε_{IR} is spectral emissivity for infrared thermograph, and C and n are constants which depend on wavelength of infrared radiation and so forth. For a blackbody, the noise amplitude of the emissive power can be expressed as follows:

$$\Delta E_{IR0}(T) = C(T + \Delta T_{IR0})^n - C T^n \,. \tag{36}$$

Similarly, for a non-blackbody, the noise amplitude can be expressed as follows:

$$\Delta E_{IR}(T) = \varepsilon_{IR} C(T + \Delta T_{IR})^n - \varepsilon_{IR} C T^n \,. \tag{37}$$

Since the noise intensity is independent of spectral emissivity ε_{IR}, the values of $\Delta E_{IR0}(T)$ and $\Delta E_{IR}(T)$ are identical. This yields the following relation using the binomial theorem with the assumption of $T >> \Delta T_{IR0}$ and $T >> \Delta T_{IR}$.

$$\Delta T_{IR} = \Delta T_{IR0} / \varepsilon_{IR} \,. \tag{38}$$

Namely, the temperature resolution (NETD) for a non-blackbody is inversely proportional to ε_{IR}.

4.2 Upper limit of fluctuating frequency

Using Eq. (20) – (24) and (26), the fluctuating amplitude, $(\Delta T_w)_f$, is generally expressed as follows for higher fluctuating frequency:

$$(\Delta T_w)_f \approx \frac{(\overline{T_w} - T_0)\Delta h}{2\pi c\rho\delta f + \sqrt{\pi c_i \rho_i \lambda_i} f^{0.5}} \,, \quad (\tilde{f} > 4 \text{ and } k_i\delta_i >> 1) \tag{39}$$

The fluctuation is detectable using infrared thermography for $(\Delta T_w)_f > \Delta T_{IR}$. This yields the following equation from Eq. (38) and (39).

$$f < \left(\frac{-B + \sqrt{B^2 - 4AC}}{2A} \right)^2 \,, \quad A = 2\pi c\rho\delta \,, \; B = \sqrt{\pi c_i \rho_i \lambda_i} \,, \; C = -\varepsilon_{IR} \Delta h (\overline{T_w} - T_0) / \Delta T_{IR0} \tag{40}$$

The maximum frequency of Eq. (40) at $(\Delta T_w)_f = \Delta T_{IR}$ corresponds to the upper limit of the detectable fluctuating frequency, f_{max}. The value of f_{max} is uniquely determined as a function of $\Delta h(\overline{T_w} - T_0) / \Delta T_{IR0}$ if the thermophysical properties of the thin foil and the insulating layer are specified.

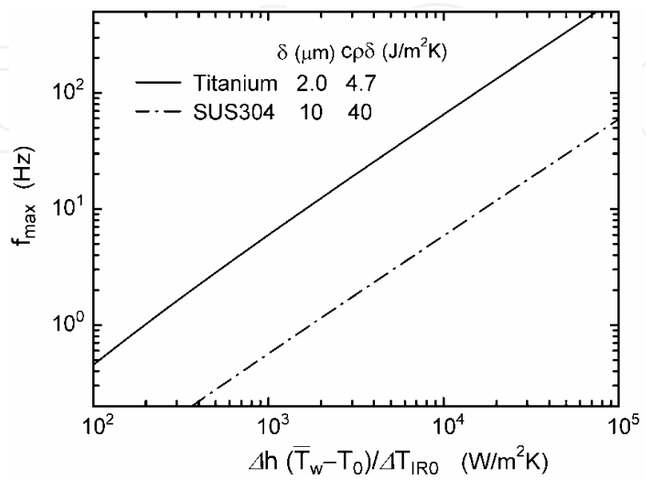

Fig. 6. Upper limit of the fluctuating frequency detectable using infrared measurements

Figure 6 shows the relation of f_{max} for practical metallic foils for heat transfer measurement to air, namely, a titanium foil of 2 μm thick ($c\rho\delta$ = 4.7 J/m²K, ε_{IR} = 0,2) and a stainless-steel foil of 10 μm thick ($c\rho\delta$ = 40 J/m²K, ε_{IR} = 0.15). The insulating layer is assumed to be a still air layer (c_i = 1007 J/kg·K, ρ_i = 1.18 kg/m³, λ_i = 0.0265 W/m·K), which has low heat capacity and thermal conductivity.

For example, a practical condition likely to appear in flow of low-velocity turbulent air (section 6; $\Delta h(\overline{T_w} - T_0) / \Delta T_{IR0}$ = 22000 W/m²K; Δh = 20 W/m²K, $\overline{T_w} - T_0$ = 20 K, and ΔT_{IR0} = 0.018 K), gives the values f_{max} = 150 Hz for the 2 μm thick titanium foil. Therefore, the unsteady heat transfer caused by flow turbulence can be detected using this measurement technique, if the flow velocity is relatively low (see section 6).

The value of f_{max} increases with decreasing $c\rho\delta$ and ΔT_{IR0}, and with increasing ε_{IR}, Δh, and $\overline{T_w} - T_0$. The improvements of both the infrared thermograph (decreasing ΔT_{IR0} with increasing frame rate) and the thin foil (decreasing $c\rho\delta$ and/or increasing ε_{IR}) will improve the measurement.

4.3 Upper limit of spatial wavenumber

Using Eq. (29) – (32) and (34), the spatial amplitude, $(\Delta T_w)_s$, is generally expressed as follows for higher wavenumber:

$$(\Delta T_w)_s \approx \frac{(\overline{T_w} - T_0)\Delta h}{\lambda\delta k^2 + \lambda_i k} \quad , \quad (\tilde{k} > 4 \text{ and } k\delta_i >> 1). \tag{41}$$

The spatial distribution is detectable using infrared thermography for $(\Delta T_w)_s > \Delta T_{IR}$. This yields the following equation using Eq. (38) and (41).

$$k < \frac{-\lambda_i + \sqrt{\lambda_i^2 + 4\lambda\delta\,\varepsilon_{IR}\{\Delta h(\overline{T_w} - T_0) / \Delta T_{IR0}\}}}{2\lambda\delta} \tag{42}$$

The maximum wavenumber of Eq. (42) at $(\Delta T_w)_s = \Delta T_{IR}$ corresponds to the upper limit of the detectable spatial wavenumber, k_{max}. If thermophysical properties of the thin foil and the

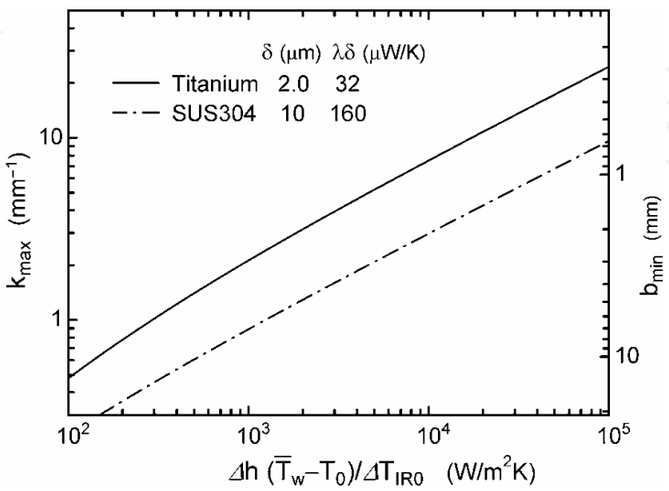

Fig. 7. Upper limit of the spatial wavenumber detectable using infrared measurements

insulating layer are specified, the value of k_{max} is uniquely determined as a function of $\Delta h(\overline{T_w} - T_0) / \Delta T_{IR0}$, as well as f_{max}.

Figure 7 shows the relation for k_{max} for the titanium foil of 2 μm thickness ($\lambda\delta$ = 32 μW/K, ε_{IR} = 0.2), and the stainless-steel foil of 10 μm thickness ($\lambda\delta$ = 160 μW/K, ε_{IR} = 0.15). The insulating layer is assumed to be a still-air layer (λ_i = 0.0265 W/m·K). For example, at a practical condition appeared in section 6, $\Delta h(\overline{T_w} - T_0) / \Delta T_{IR0}$ = 22000 W/m²K, the value of k_{max} (b_{min}) is 11 mm^{-1} (0.6 mm) for the 2 μm thick titanium foil. Therefore, the spatial structure of the heat transfer coefficient caused by flow turbulence can be detected using this measurement technique. (In general, the space resolution is dominated by rather a pixel resolution of infrared thermograph than k_{max} (b_{min}), see Nakamura, 2007b).

The value of k_{max} increases with decreasing $\lambda\delta$ and ΔT_{IR0}, and with increasing ε_{IR}, Δh, and $\overline{T_w} - T_0$. The improvements of both the infrared thermograph (decreasing ΔT_{IR0} with increasing pixel resolution) and the thin foil (decreasing $\lambda\delta$ and/or increasing ε_{IR}) will improve the measurement.

5. Experimental demonstration (turbulent boundary layer)

In this section, the applicability of this technique was verified by measuring the spatio-temporal distribution of the heat transfer on the wall of a turbulent boundary layer, as a well-investigated case.

5.1 Experimental setup

The measurements were performed using a wind tunnel of 400 mm (H) × 150 mm (W) × 1070 mm (L), as shown in Fig. 8. A turbulent boundary layer was formed on the both-side faces of a flat plate set at the mid-height of the wind tunnel. The freestream velocity u_0 ranged from 2 to 6 m/s, resulting in the Reynolds number based on the momentum thickness was Re_θ = 280 – 930.

The test plate fabricated from acrylic resin (6 mm thick, see Fig. 8 (c)) had a removed section, which was covered with a titanium foil of 2 μm thick on both the lower and upper faces. Both ends of the foil was closely adhered to electrodes with high-conductivity bond to suppress a contact resistance. A copper plate of 4 mm thick was placed at the mid-height of the removed section (see Fig. 8 (b)), to impose a thermal boundary condition of a steady and uniform temperature. On the surface of the copper plate, a gold leaf (0.1 μm thick) was glued to suppress the thermal radiation. The titanium foil was heated by applying a direct current under conditions of constant heat flux so that the temperature difference between the foil and the freestream to be about 30°C. Since both the upper and lower faces of the test plate were heated, the heat conduction loss to inside the plate was much reduced. Under these conditions, air enclosed by both the titanium foil and the copper plate does not convect because the Rayleigh number is below the critical value.

To suppress a deformation of the heated thin-foil due to the thermal expansion of air inside the plate, thin relief holes were connected from the ail-layer to the atmosphere. Also, the titanium foil was stretched by heating it since the thermal expansion coefficient of the titanium is smaller than that of the acrylic resin. This suppressed mechanical vibration of the foil against the fluctuating flow. [The amplitude of the vibration measured using a laser displacement meter was an order of 1 μm at the maximum freestream velocity of u_0 = 6 m/s. This amplitude was one or two orders smaller than the wall-friction length of the turbulent boundary layer].

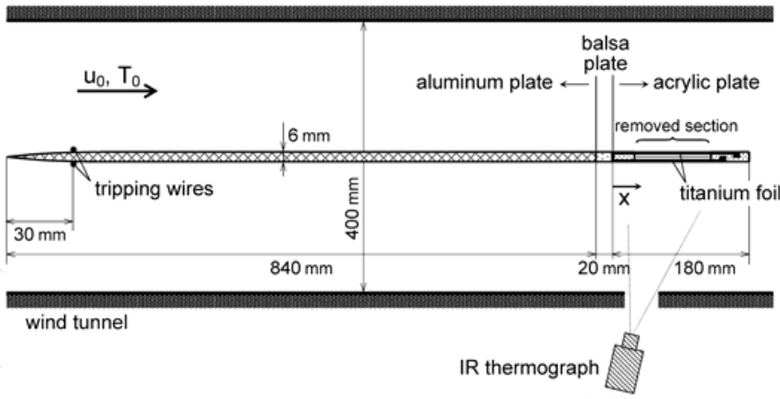

(a) Cross sectional view of the wind tunnel

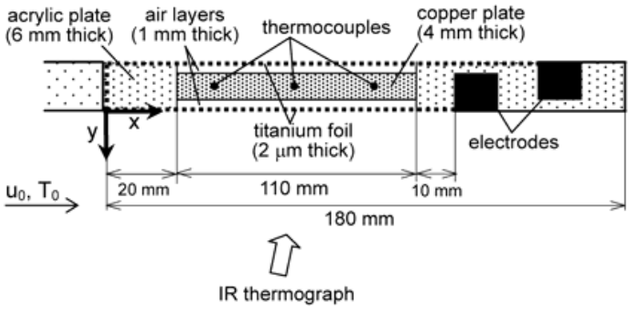

(b) Cross sectional view of the test plate

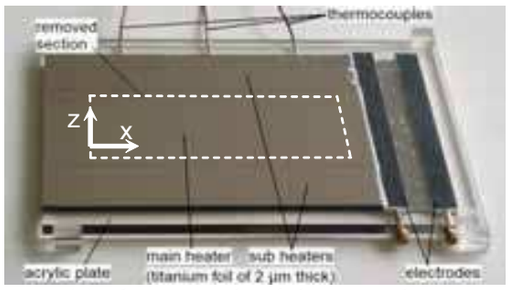

(c) Photograph of the test plate

Fig. 8. Experimental setup (turbulent boundary layer)

The infrared thermograph was positioned below the plate and it measured the fluctuation of the temperature distribution on the lower-side face of the plate. The infrared thermograph used in this section (TVS-8502, Avio) can capture images of the instantaneous temperature distribution at 120 frames per second, and a total of 1024 frames with a full resolution of 256×236 pixels. The value of NETD of the infrared thermograph for a blackbody was ΔT_{IR0} = 0.025 K.

The temperature on the titanium foil T_w was calculated using the following equation:

$$E_{IR} = \varepsilon_{IR} f(T_w) + (1 - \varepsilon_{IR}) f(T_a) \tag{43}$$

Here, E_{IR} is the spectral emissive power detected by infrared thermograph, $f(T)$ is the calibration function of the infrared thermograph for a blackbody, ε_{IR} is spectral emissivity for the infrared thermograph, and T_a is the ambient wall temperature. The first and second terms of the right side of Eq. (43) represent the emissive power from the test surface and surroundings, respectively. In order to suppress the diffuse reflection, the inner surface of the wind tunnel (the surrounding surface of the test surface) was coated with black paint. Also, in order to keep the second term to be a constant value, careful attention was paid to keep the surrounding wall temperature to be uniform. The thermograph was set with an inclination angle of 20° against the test surface in order to avoid the reflection of infrared radiation from the thermograph itself.

The spectral emissivity of the foil, ε_{IR}, was estimated using the titanium foil, which was adhered closely to a heated copper plate. The value of ε_{IR} can be estimated from Eq. (43) by

substituting E_{IR} detected by the infrared thermograph, the temperature of the copper plate ($\approx T_w$) measured using such as thermocouples, and the ambient wall temperature T_a.

The accuracy of this measurement was verified to measure the distribution of mean heat transfer coefficient of a laminar boundary layer. The result was compared to a 2D heat conduction analysis assuming the velocity distribution to be a theoretical value. The agreement was very well (within 3 %), indicating that the present measurement is reliable to evaluate the heat transfer coefficient at least for a steady flow condition (Nakamura, 2007a and 2007b).

Also, a dynamic response of this measurement was investigated against a stepwise change of the heat input to the foil in conditions of a steady flow for a laminar boundary layer. The response curve of the measured temperature agreed well to that of the numerical analysis of the heat conduction equation. This indicates that the delay due to the heat capacity of the foil, $c\rho\delta(\partial T_w / \partial t)$ in Eq. (44), and the heat conduction loss to the air-layer, $\dot{q}_{cd} = \lambda_a (\partial T/\partial y)_{y=0-}$ in Eq.(44), can be evaluated with a sufficient accuracy (Nakamura, 2007b).

5.2 Spatio-temporal distribution of temperature

Figure 9 (a) and (b) shows the results of the temperature distribution of laminar and turbulent boundary layers, respectively, measured using infrared thermography. The freestream velocity was u_0 = 3 m/s for both cases. Bad pixels existed in the thermo-images were removed by applying a 3×3 median filter (here, intermediate three values were averaged). Also, a low-pass filter (sharp cut-off) was applied in order to remove a high frequency noise more than f_c = 30 Hz (corresponds to less than 4 frames) and the small-scale spatial noise less than b_c = 3.4 mm (corresponds to less than 6 pixels).

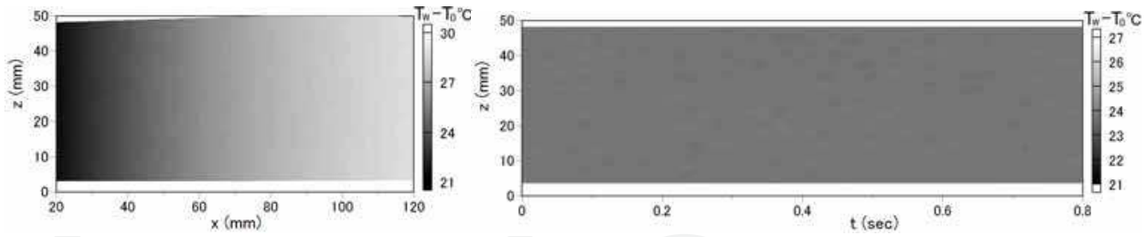

(a) Laminar boundary layer at u_0 = 3 m/s; Right – spanwise time trace at x = 37 mm

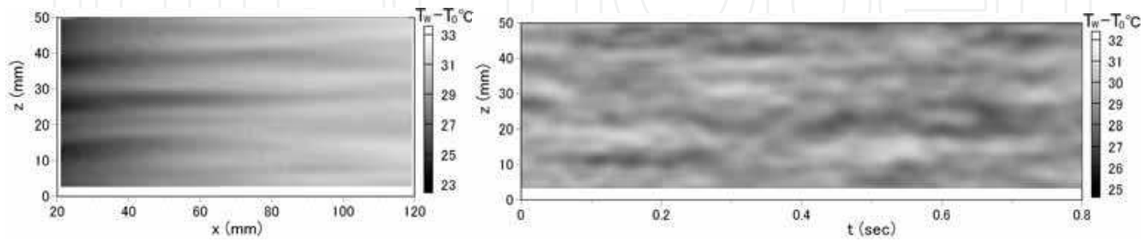

(b) Turbulent boundary layer at u_0 = 3 m/s; Re_θ = 530; Right – spanwise time trace at x = 69mm

Fig. 9. Temperature distribution T_w–T_0 measured using infrared thermography

As depicted in Figure 9 (b), the temperature for the turbulent boundary layer has large nonuniformity and fluctuation according to the flow turbulence. The thermal streaks appear

in the instantaneous distribution, which extend to the streamwise direction. Figure 10 shows the power spectrum of the temperature fluctuation. The S/N ratio of the measurement estimated based on the power spectrum for the laminar boundary layer (noise) was 500 – 1000 (27 – 30 dB) in the lower frequency range of 0.4 – 6 Hz and about 10 (10 dB) at the maximum frequency of f_c = 30 Hz after applying the filters.

5.3 Restoration of heat transfer coefficient

The local and instantaneous heat transfer coefficient was calculated using the following equation derived from the heat conduction equation in a thin foil (Eq. (1) – (3)).

$$h = \frac{\dot{q}_{in} - \dot{q}_{cd} - \dot{q}_{rd} - \dot{q}_{rdi} + \lambda\delta\left(\frac{\partial^2 T_w}{\partial x^2} + \frac{\partial^2 T_w}{\partial z^2}\right) - c\rho\delta\frac{\partial T_w}{\partial t}}{T_w - T_0} \tag{44}$$

This equation contains both terms of lateral conduction through the foil, $\lambda\delta(\partial^2 T_w/\partial x^2 + \partial^2 T_w/\partial z^2)$, and the thermal inertia of the foil, $c\rho\delta(\partial T_w/\partial t)$. Heat conduction to the air layer inside the foil, $\dot{q}_{cd} = \lambda_a (\partial T/\partial y)_{y=0-}$, was calculated using the temperature distribution in the air layer, which can be determined by solving the heat conduction equation as follows (the coordinate system is shown in Fig. 8):

$$c_a\rho_a\frac{\partial T}{\partial t} = \lambda_a\left(\frac{\partial^2 T}{\partial x^2} + \frac{\partial^2 T}{\partial y^2} + \frac{\partial^2 T}{\partial z^2}\right), \ (-\delta_a < y < 0) \tag{45}$$

Here, c_a, ρ_a and λ_a are specific heat, density and thermal conductivity of air (This Equation is similar to Eq. (7) only the subscript i is replaced to a). Since the temperature of the copper plate inside the test plate is assumed to be steady and uniform, the boundary condition of Eq. (45) on the copper plate side ($y = -\delta_a$) can be assumed as a mean temperature of the copper plate measured using thermocouples.

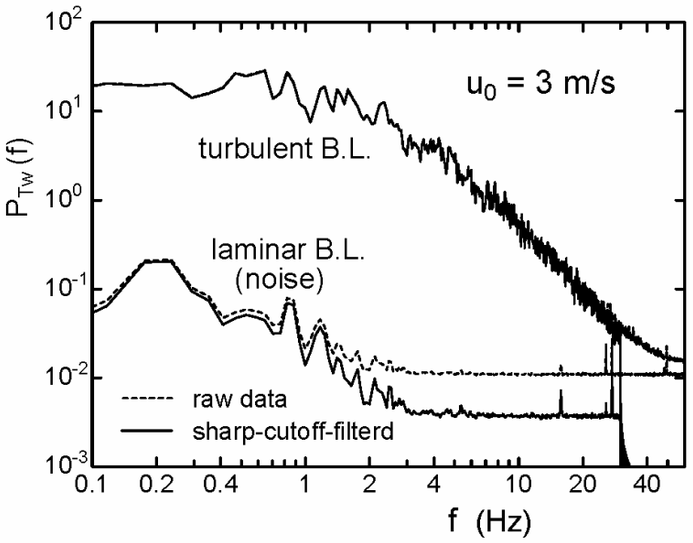

Fig. 10. Power spectrum of temperature fluctuation appeared in Fig. 9

The finite difference method was applied to calculate the heat transfer coefficient h from Eq. (44) and (45). Time differential Δt corresponded to the frame interval of the thermo-images (in this case, Δt = 1/120 s = 8.3 ms). Space differentials Δx and Δz corresponded to the pixel pitch of the thermo-image (in this case, $\Delta x \approx \Delta z \approx 0.56$ mm). The thickness of the air layer (δ_a = 1 mm) was divided into two regions (Δy = 0.5 mm). [In this case, normal temperature distribution in the air-layer can be assumed to linear within an interval of Δy = 0.5 mm up to the maximum frequency of f_c = 30 Hz, since it satisfies $\kappa_a \Delta y < 1$; see section 3.1] Eq. (45) was solved using ADI (alternative direction implicit) method (Peaceman and Rachford, 1955) with respect to x and z directions.

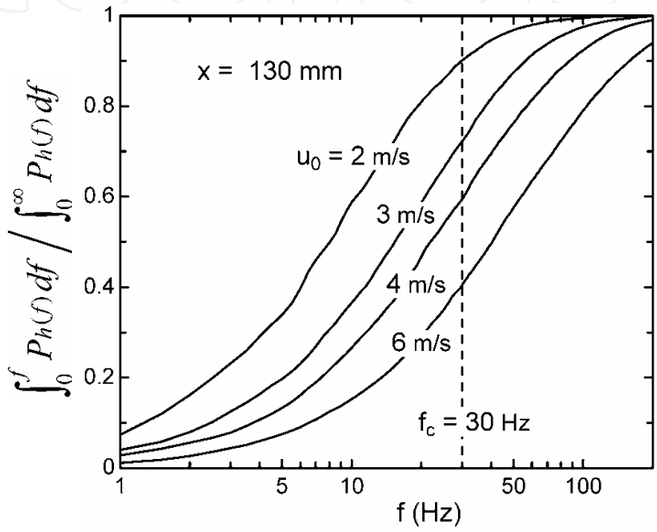

Fig. 11. Cumulative power spectrum of fluctuating heat transfer coefficient

The above procedure (the finite different method including the median and the sharp cut-off filters) restored the heat transfer coefficient up to f_c = 30 Hz in time with the attenuation rate of below 20 % and up to b_c = 3.4 mm in space with the attenuation rate of below 30 % (Nakamura, 2007b). The wavelength of b_c = 3.4 mm corresponded to 20 – 48 l_τ (for u_0 = 2 – 6 m/s), which was smaller than the mean space between the thermal streaks (≈ 100 l_τ , see Fig. 14).

Figure 11 shows cumulative power spectrum of the fluctuation of the heat transfer coefficient measured using a heat flux sensor (HFM-7E/L, Vatell; time constant faster than 3 kHz) under a condition of steady wall temperature. For the freestream velocity u_0 = 2 m/s, the fluctuation energy below f_c = 30 Hz accounts for 90 % of the total energy, indicating that the fluctuation can be restored almost completely by the above procedure. However, with an increase in the freestream velocity, the ratio of the fluctuation energy below f_c = 30 Hz decreases, resulting in an insufficient restoration.

5.4 Spatio-temporal distribution of heat transfer

The spatio-temporal distribution of the heat transfer coefficient restored using the above procedure is shown in Fig. 12. The features of the thermal streaks are clearly revealed, which extend to the streamwise direction with small spanwise inclinations. The heat transfer coefficient fluctuates vigorously showing a quasi-periodic characteristic in both time and

spanwise direction, which is reflected by the unique behavior of the thermal streaks. Although the restoration for u_0 = 3 m/s (Fig. 12 (b)) is not sufficient, as shown in Fig. 11, the characteristic scale of the fluctuation seems to be smaller both in time and spanwise direction than that for u_0 = 2 m/s, indicating that the structure of the thermal streaks becomes finer with increasing the freestream velocity.

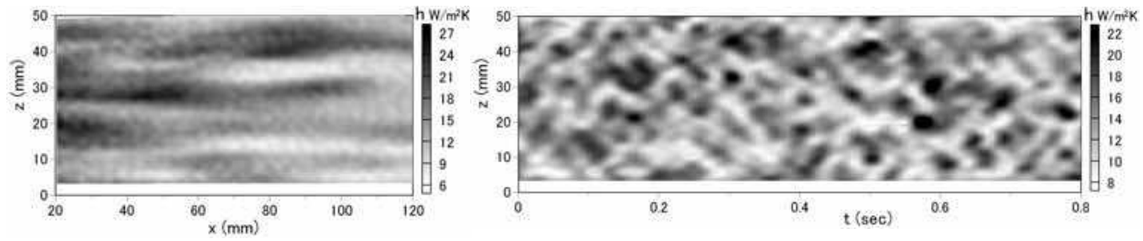

(a) u_0 = 2 m/s, Re_θ = 280, l_τ = 0.174 mm; Right – spanwise time trace at x = 69 mm

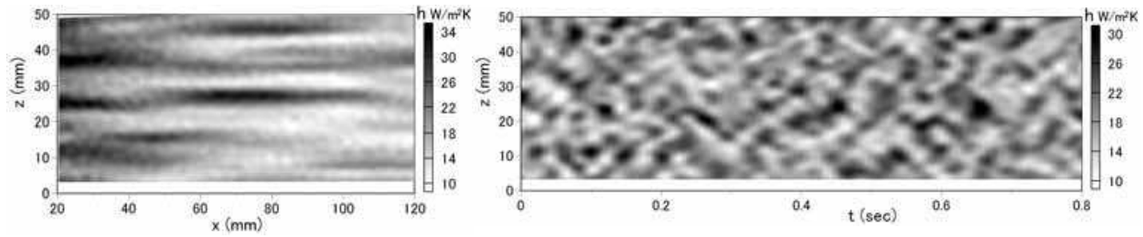

(b) u_0 = 3 m/s, Re_θ = 530, l_τ = 0.126 mm; Right – spanwise time trace at x = 69 mm

Fig. 12. Time-spatial distribution of heat transfer coefficient (turbulent boundary layer)

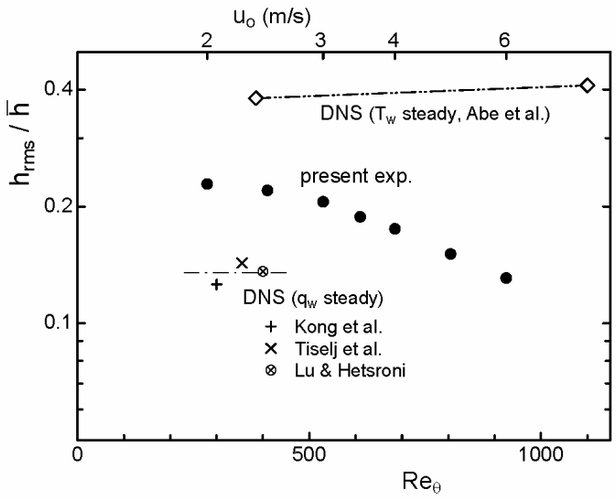

Fig. 13. Rms value of the fluctuating heat transfer coefficient at x = 69 mm

Figure 13 plots the rms value of the fluctuation $h_{rms}/\overline{h}$ at x = 69 mm. The value at u_0 = 2 m/s (Re_θ = 280) was $h_{rms}/\overline{h}$ = 0.23, at which the restoration is almost complete. However, it decreases with increasing the freestream velocity due to the insufficient restoration. For u_0 = 2 m/s, the value of f_{max} is 37 Hz (see section 4.2), while the frequency restored is f_c = 30 Hz. This indicates that the restoration up to $f_c \approx f_{max}$ is possible without exaggerating the noise.

The results of direct numerical simulation (Lu and Hetsroni, 1995, Kong et al, 2000, Tiselj et al, 2001, and Abe et al, 2004) are also plotted in Fig. 13. As shown in this Figure, the value of $h_{rms}/\overline{h}$ greatly depends on the difference in the thermal boundary condition, that is, $h_{rms}/\overline{h}$ ≈ 0.4 for steady temperature condition (corresponds to infinite heat capacity wall), whereas $h_{rms}/\overline{h}$ = 0.13 – 0.14 for steady heat flux condition (corresponds to zero heat capacity wall). Since the present experiment was performed between two extreme conditions, for which the temperature on the wall fluctuates with a considerable attenuation, the value $h_{rms}/\overline{h}$ = 0.23 seems to be reasonable.

Figure 14 plots the mean spanwise wavelength of the thermal streak, $l_z^+ = l_z/l_\tau$, which is determined by an auto-correlation of the spanwise distribution. For the lower velocity of u_0 = 2 – 3 m/s (Re_θ = 280 – 530), the mean wavelength is l_z^+ = 77 – 87, which agrees well to that for the previous experimental data obtained using water as a working fluid (Iritani et al, 1983 and 1985, and Hetsroni & Rozenblit, 1994; l_z^+ = 74 – 89). This wavelength is smaller than that for DNS (Kong et al, 2000, Tiselj et al, 2001, and Abe et al, 2004; l_z^+ = 100 – 150), probably due to the additional flow turbulence in the experiments, such as freestream turbulence. The value of l_z^+ for the present experiment increases with increasing the Reynolds number, the reason of which is not clear at present.

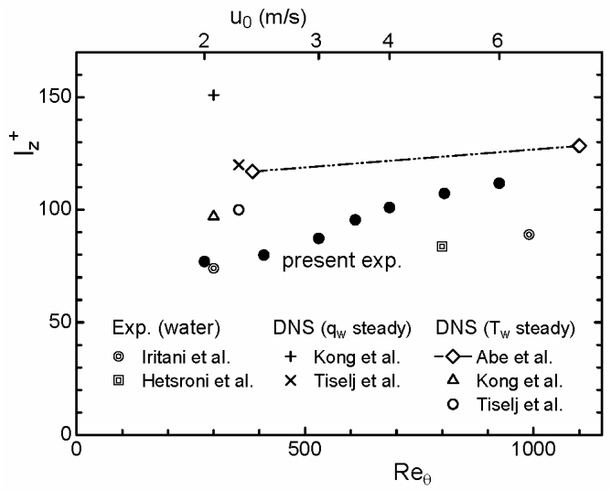

Fig. 14. Mean spanwise wavelength of thermal streaks

In this section, the time-spatial heat transfer coefficient was restored up to 30 Hz in time and 3.4 mm in space at a low heat transfer coefficient of $\overline{h}$ = 10 – 20 W/m²K, by employing a 2 μm thick titanium foil and an infrared thermograph of 120 Hz with NETD of 0.025K. This restoration was, however, not exactly sufficient, particularly for the higher freestream velocity of u_0 > 2 m/s. Yet, the higher frequency fluctuation will be restored by employing the higher-performance thermograph (higher frame rate with lower NETD, see section 6), if a condition of $f_c < f_{max}$ is satisfied.

6. Experimental demonstration (separated and reattaching flow)

The recent improvement of infrared thermograph with respect to temporal, spatial and temperature resolutions enable us to investigate more detailed behavior of the heat transfer caused by flow turbulence. In this section, the heat transfer behind a backward-facing step

which represents the separated and reattaching flow was explored by employing a higher-performance thermograph. Special attention was devoted to investigate the spatio-temporal characteristics of the heat transfer in the flow reattaching region.

6.1 Experimental setup

Figure 15 shows the test plate used here. The wind tunnel and the flat plate (aluminum plate) is the same as that used in section 5 (see Fig. 8). A turbulent boundary layer was formed on the lower-side face of the flat plate (aluminum plate) followed by a step. The step height was H = 5, 10 and 15.6 mm, thus the aspect ratio was AR = 30, 15, and 9.6 and the expansion ratio was ER = 1.025, 1.05 and 1.08, respectively. The freestream velocity ranged from 2 to 6 m/s, resulting in the Reynolds number based on the step height was Re_H = 570 – 5400.

The test plate fabricated from acrylic resin (6 mm thick) had two removed sections (see Fig. 15 (b)), which were covered with two sheets of titanium foil of 2 μm thick on both the lower and upper faces. A copper plate of 4 mm thick was placed at the mid-height of each removed section. The titanium foil was heated by applying a direct current so that the temperature difference between the foil and the freestream was around 20–30°C. The amplitude of the mechanical vibration of the foil in the flow reattaching region measured using a laser displacement meter was an order of 1 μm at the maximum freestream velocity of u_0 = 6 m/s.

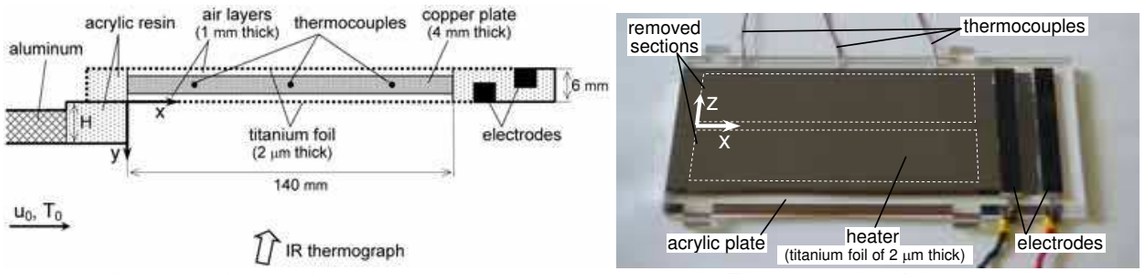

(a) Cross sectional view around the step (b) Photograph of the test plate

Fig. 15. Experimental setup (backward-facing step)

In this study, a high-speed infrared thermograph of SC4000, FLIR (420 frames per second with a resolution of 320×256 pixels, or 800 frames per second with a resolution of 192×192 pixels, NETD of 0.018 K) was employed in addition to TVS-8502, AVIO (see section 5).

6.2 Time-averaged distribution

Figure 16 shows streamwise distribution of Nusselt number, $Nu_H = \bar{h}H / \lambda$, where $\bar{h}$ is time and spanwise-averaged heat transfer coefficient calculated from the time-spatial distribution of the heat transfer coefficient (shown later in Fig. 20). The x axis is originated from the step. The Nusselt number was normalized by $Re_H^{2/3}$, because the local Nusselt number of the separated and reattaching flows usually proportional to $Re^{2/3}$ (Richardson, 1963; Igarashi, 1986). For the present experiment, the distribution of $Nu_H/Re^{2/3}$ almost corresponded for Re_H > 2000, as shown in Fig. 16.

The Nusselt number distribution has a similar trend as that investigated previously (Vogel and Eaton, 1985; among others); it increases sharply toward the flow reattachment zone ($x/H \approx 5$ for the present experiment), and then it decreases gradually with a development to a turbulent boundary layer. The difference in the peak location of the distribution can be

explained by the fact that it moves downstream with an increase in the expansion ratio (*ER*), as indicated by Durst and Tropea, 1981. Also, it moves upstream with an increase in the turbulent boundary layer thickness upstream of the step (Eaton and Johnston, 1981).

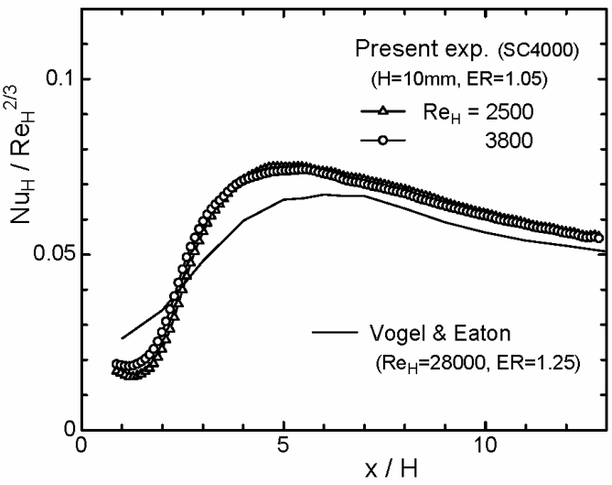

Fig. 16. Streamwise distribution of Nusselt number for the backward-facing step

6.3 Spatio-temporal distribution

Figure 17 shows examples of an instantaneous distribution of temperature on the titanium foil as measured using infrared thermograph (SC4000). The step height was H = 10 mm and the freestream velocity was u_0 = 6 m/s, resulting in the Reynolds number of Re_H = 3800. Bad pixels in the thermo-images were removed by applying a 3×3 median filter (here, intermediate three values were averaged). Also, a low-pass filter (sharp cut-off) was applied in order to remove a high frequency noise (more than f_c = 53 Hz for the wide measurement of Fig. 17 (a) and more than f_c = 133 Hz for the close-up measurement of Fig. 17 (b)) and the small-scale spatial noise (less than b_c = 4.9 mm for the wide measurement and less than b_c = 2.2 mm for the close-up measurement).

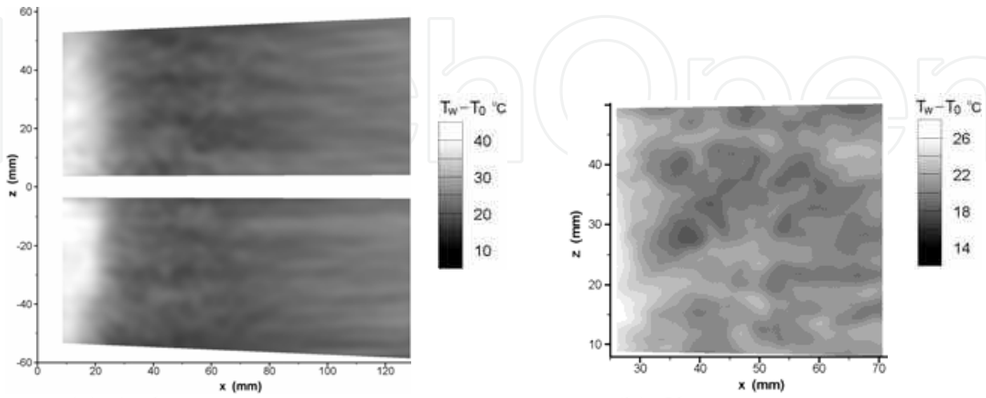

(a) Wide measurement (420 Hz, 320 × 256 pixels)

(b) Close-up measurement (800 Hz, 192 × 192 pixels)

Fig. 17. Temperature distribution T_w–T_0 behind the backward-facing step (H = 10 mm, u_0 = 6 m/s, Re_H = 3800; step at x = 0)

Incidentally, the upper limit of the detectable fluctuating frequency (f_{max}, see section 4.2) and the lower limit of the detectable spatial wavelength (b_{min}, see section 4.3) in the reattachment region at u_0 = 6 m/s are f_{max} = 150 Hz and b_{min} = 0.6 mm (Δh = 20 W/m²K, $\overline{T_w} - T_0$ = 20°C, ΔT_{IR0} = 0.018 K, for a 2 μm thick titanium foil). Therefore, both the cutoff frequency of f_c = 133 Hz and the cutoff wavelength of b_c = 2.2 mm are within the detectable range.

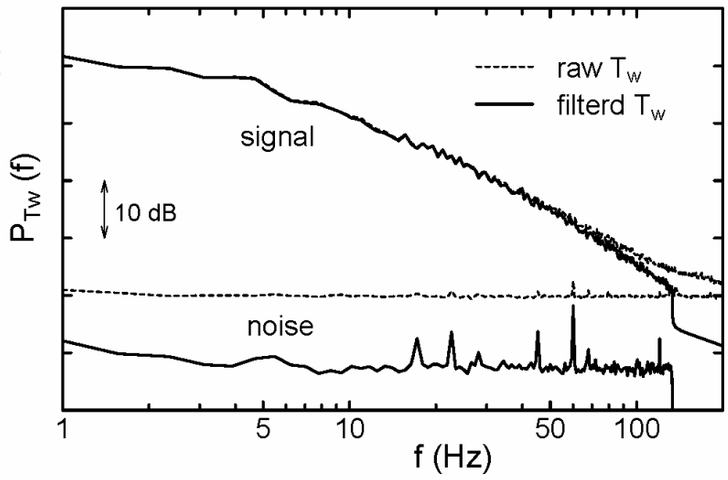

Fig. 18. Power spectrum of the temperature fluctuation: signal – temperature at x = 50 mm; noise – temperature on a steady temperature plate

Figure 18 shows power spectrums for both signal and noise of the temperature detected by the infrared thermograph (SC4000) for the close-up measurement. The noise was estimated by measuring the temperature on the titanium foil glued on a copper plate. The noise was much reduced by about 10 dB by applying the median and the low-pass filters, resulting that the S/N ratio of the measurement was greater than 1000 for f < 30 Hz and 10-20 at the maximum frequency of f_c = 133 Hz.

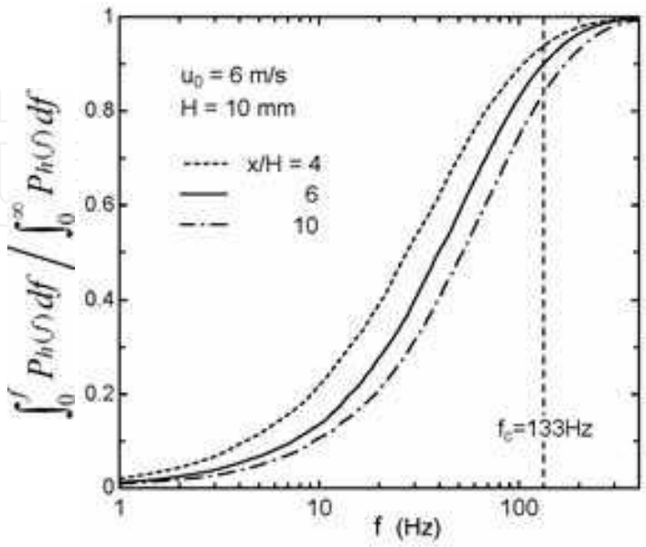

Fig. 19. Cumulative power spectrum of fluctuating heat transfer coefficient

Figure 19 shows a cumulative power spectrum of the fluctuation of the heat transfer coefficient in the flow reattaching region measured using a heat flux sensor (HFM-7E/L, Vatell; time-constant faster than 3 kHz) under a condition of steady wall temperature (its power spectrum is shown later in Fig. 22 (b)). As indicated in Fig. 19, the most part of the fluctuating energy of the heat transfer coefficient (about 90 %) can be restored at the cutoff frequency of f_c = 133 Hz for the maximum velocity of u_0 = 6 m/s.

The spatio-temporal distribution of the heat transfer coefficient corresponding to Fig. 17 (a) and (b) is shown in Figs. 20 and 21, respectively, which were calculated by the similar procedure to that described in section 5.3. These figures reveal some unique characteristics of time-spatial behavior of the heat transfer for the separated and reattaching flow, which has hardly been clarified in the previous experiments. The most impressive feature is that the heat transfer enhancement in the reattachment zone (x = 30 – 70 mm) has a spot-like characteristic, as shown in the instantaneous distribution (Fig. 20 (a) and 21 (a)). The high heat transfer spots appear and disappear almost randomly but have some periodicity in time and spanwise direction, as indicated in the time traces (Fig. 20 (b), (c) and Fig. 21 (b), (c)). Each spot spreads with time, which forms a track of "∧" shape in the streamwise time trace (Fig. 21 (b)) corresponding to the streamwise spreading, and forms a track of "〈" shape in the spanwise time trace (Fig. 21 (c)) corresponding to the spanwise spreading. The basic behavior of the spot spreading overlaps with others to form a complex feature in the spatio-temporal characteristics of the heat transfer.

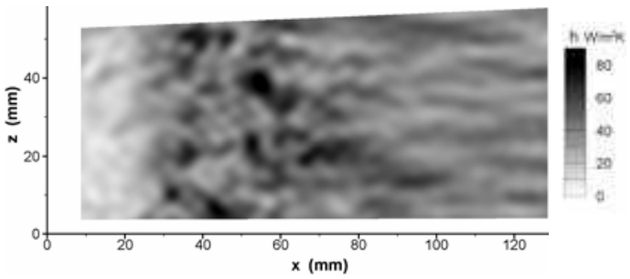

(a) Instantaneous distribution at t = 0

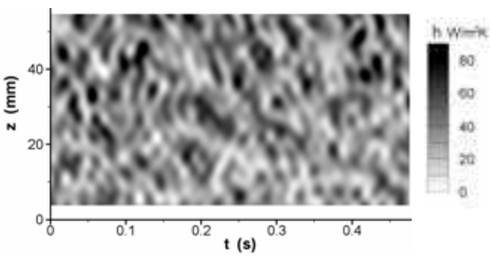

(c) Spanwise time trace at x = 50 mm

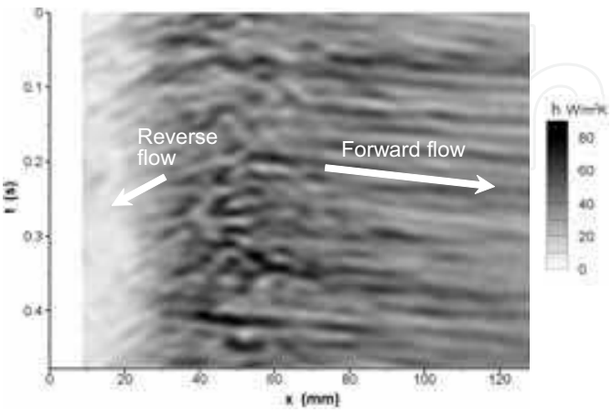

(b) Streamwise time trace at z = -10 mm

Fig. 20. Time-spatial distribution of heat transfer coefficient behind the backward-facing step (H = 10 mm, u_0 = 6 m/s, Re_H = 3800; f_c = 53 Hz, b_c = 4.9 mm)

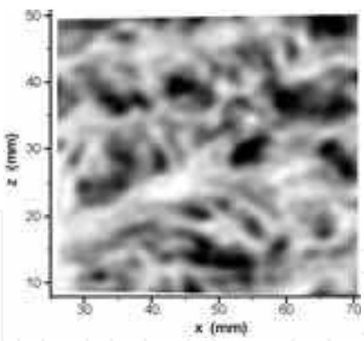

(a) Instantaneous distribution at t = 0

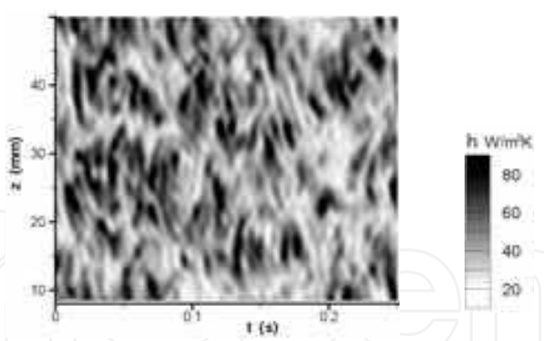

(c) Spanwise time trace at x = 50 mm

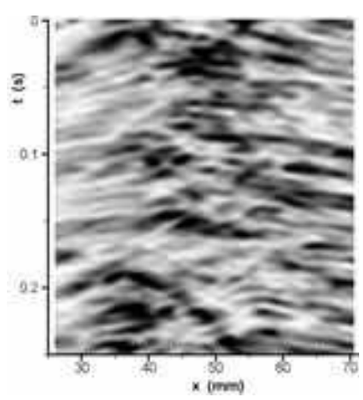

(b) Streamwise time trace at z = 29 mm

Fig. 21. Time-spatial distribution of heat transfer coefficient around the reattaching region (H = 10 mm, u_0 = 6 m/s, Re_H = 3800; f_c = 133 Hz, b_c = 2.2 mm)

The heat transfer coefficient is considerably low beneath the separation region, which is formed between the step and the flow reattachment zone (x < 30 mm, see Fig. 20 (a)). The reverse flow occurs from the reattachment zone to this region (x = 30 – 10 mm), which is depicted by tracks of high heat transfer regions as shown in the streamwise time trace (Fig. 20 (b)). The velocity of the reverse flow, which was determined by the slope of the tracks, was very slow, approximately 0.05 – 0.1 of the freestream velocity.

Behind the flow reattachment zone (x > 70 mm), the flow gradually develops into a turbulent boundary layer flow. The spot-like structure in the reattachment zone gradually change it form to streaky-structure, as can be seen in the instantaneous distribution of Fig. 20 (a). The characteristic velocity of this structure, which was determined by the slope of the tracks of the streamwise time trace (Fig. 20 (b)), was roughly $0.5u_0$, which varies widely as can be seen in the fluctuation of the tracks. This velocity was similar to the convection speed of vortical structure near the reattachment zone ($0.5u_0$ for Kiya & Sasaki, 1983 and $0.6u_0$ for Lee & Sung, 2002). Kawamura et al., 1994 also indicated that the convection speed of the heat transfer structure is approximately $0.5u_0$ for the constant-wall-temperature condition.

6.4 Temporal characteristics

Figure 22 (a) shows time traces of the fluctuating heat transfer coefficient in the reattaching region measured using the heat flux sensor (HFS) and the infrared thermograph (IR).

Although the time trace of IR does not have sharp peaks as that of HFS probably due to the low-pass filter of f_c = 133Hz, the basic characteristics of the fluctuation seems to be similar. Figure 22 (b) shows power spectrum of the fluctuation corresponding to Fig. 22 (a). The attenuation with frequency for IR is similar to that for HFS up to the sharp-cutoff frequency of f_c = 133Hz, while the thermal boundary condition is different.

The previous studies have indicated that the flow in the reattaching region behind a backward-facing step was dominated by low-frequency unsteadiness. Eaton & Johnston, 1980 measured the energy spectra of the streamwise velocity fluctuations at several locations and reported that the spectral peak occurred at the Strouhal number St = 0.066 – 0.08. The direct numerical simulation performed by Le et al., 1997 also showed the dominant frequency of the velocity was roughly St = 0.06. The origin of this unsteadiness is not completely understood, but it may be caused by the pairing of the shear layer vortices (Schäfer et al., 2007).

In order to explore the effect of the low-frequency unsteadiness on the heat transfer, autocorrelation function of the time trace of Fig. 22 (a) was calculated. The result is shown in Fig. 22 (c), which has some bumps in both HFS and IR measurements. The characteristic

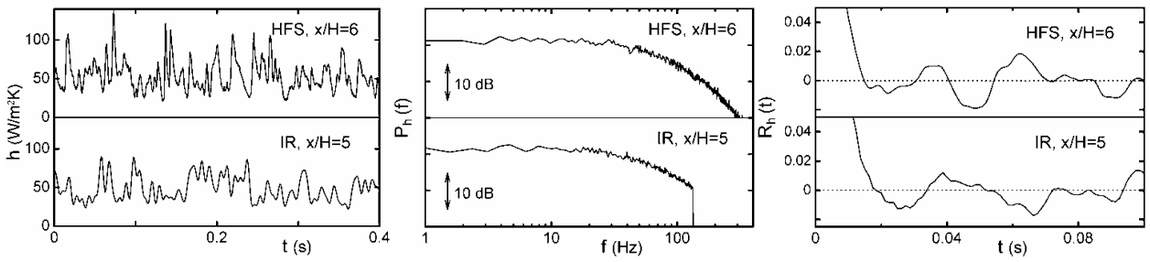

(a) Time trace (b) Power spectrum (c) Auto-correlation

Fig. 22. Fluctuation of heat transfer coefficient around the flow reattaching region (H = 10mm, u_0 = 6 m/s, Re_H = 3800)

period of the bumps is roughly 0.02s – 0.04s, corresponding to the fluctuation of St = 0.04 – 0.08. This fluctuation seems to be related to the low-frequency unsteadiness reported in the previous literature although the power spectrum for the present experiment had no dominant peak.

As shown in Fig. 21 (c), the period of 0.02s – 0.04s contains several detailed spots of high heat transfer. This suggests that the low-frequency unsteadiness is originated from a combination of several smaller vortical structures such as the shear layer vortices caused by Kelvin-Helmholtz instability, the Strouhal number of which is 0.2 – 0.4 (Bhattacharjee, 1986).

6.5 Spatial characteristics

As depicted in the spanwise time trace (Fig. 21 (c)), there seems to exist some spanwise periodicity in the heat transfer. Figure 23 shows an example of autocorrelation function of the instantaneous spanwise distribution at the reattachment zone, which is averaged in time. As shown in this figure, there is a clear minimum, at Δz = 6.3 mm in this case. This minimum, which exists for all conditions examined here, is defined to a half spanwise wavelength of $l_z/2$. The typical wavelength estimated here, l_z/H, is plotted in Fig. 24 against Reynolds number Re_H . It is remarkable that all plots are almost concentrated into a single curve regardless of the variation of the step height H. In particular, the wavelength l_z/H has almost a constant value of about 1.2 for 2000 ≤ Re_H ≤ 5500. The measurement performed by

Kawamura et al., 1994 using heat flux sensors also indicated that there is a spanwise periodicity of about 1.2*H* around the reattaching region behind a backward-facing step at Re_H = 19600. This periodicity corresponds well to that of streamwise vortices formed around the reattaching region behind a backward-facing step, observed by Nakamaru et al., 1980 in their flow visualization, in which the most frequent spanwise wavelength was about (1.2 – 1.5)*H*. This indicates that the spanwise periodicity appeared in the heat transfer is caused by the formation of the large-scale streamwise vortices, and it is reasonable to consider that the time-spatial distribution of the heat transfer in the reattaching region is dominated by the spatio-temporal behavior of the streamwise vortices.

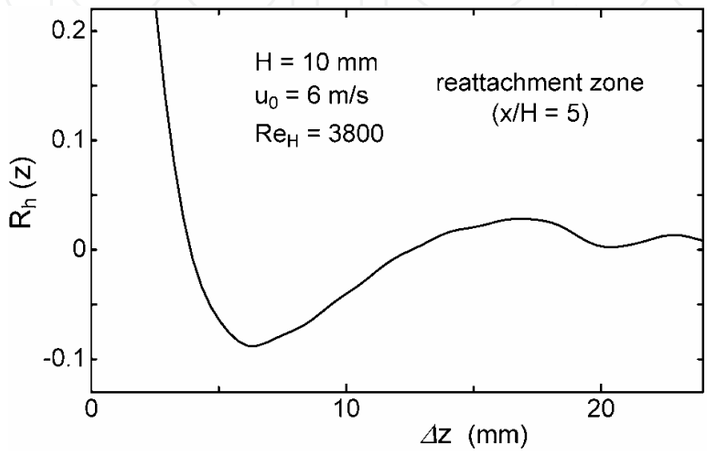

Fig. 23. Auto-correlation of instantaneous spanwise distribution of heat transfer coefficient

As shown in Fig. 24, the spanwise wavelength is closely related to the step height, not to the spacing of streaks of the turbulent boundary layer upstream of the step. This indicates that the origin of the streamwise vortices in the reattaching region is not the spanwise periodicity upstream of the step, but due to some instability behind the step, which may be accompanied by the flow separation and reattachment.

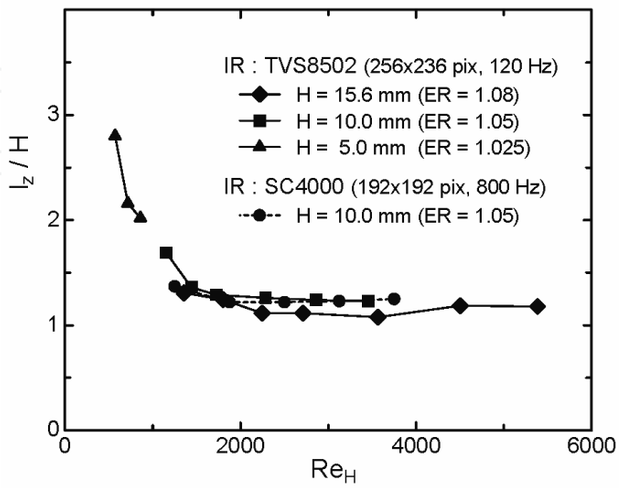

Fig. 24. Mean spanwise wavelength at the reattaching region

7. Summary and future works

In this chapter, a measurement technique was reported to explore the spatio-temporal distribution of turbulent heat transfer. This measurement can be realized using a high-speed infrared thermograph which records the temperature fluctuation on a heated thin-foil with sufficiently low heat capacity. In the existing circumstances at present, the spatial resolution of about 2 mm and the temporal resolution of about 100 Hz were possible to measure the heat transfer to air, by employ a titanium foil of 2 μm thick and a high-performance thermograph (frame rate of more than several hundred Hz and NETD of about 0.02 K). This enables us to investigate the time and spatial characteristics of turbulent heat transfer which has hardly been clarified experimentally so far.

This technique has great merits as listed below:

a. Non-intrusive measurement which does not disturb the flow and temperature fields.
b. Permits real-time observation of the spatio-temporal characteristics.
c. High spatial-resolution corresponding to the pixel pitch of the thermograph.

The spatio and temporal resolution is likely to be improved in the future with an improvement of a performance of the thermograph and a development of quality of the thin-foil.

On the other hand, there are some troublesome aspects as listed below:

d. Needs special care to treat an extremely thin foil in the fabrication and experimentation.
e. Susceptible to diffuse reflection from surroundings by using a low emissivity thin-foil.

The above terms (d. and e.) are possible to overcome as demonstrated experimentally (see sections 5 and 6). However, it is desirable to develop a thin-foil, which has a higher emissivity and an enough rigidity and elasticity.

Only a few examples were reported here concerning the forced convection heat transfer to air, yet, this technique is also available to measure the heat transfer for natural convection or mixed convection. Moreover, this technique will be extended to a liquid flow or a multiphase flow, which will be possible by measuring the temperature from the rear of the foil (from the air side), and by using a thin-foil of several tens micro-meter thick to suppress a deformation against the fluid pressure (refer to Hetsroni & Rozenblit, 1994, and Oyakawa, et al., 2000). [Ideally, the frequency-response and spatial-resolution does not deteriorate by using a foil of ten times thick if the heat transfer coefficient becomes ten times higher; see Eq. (9) and (15)].

In the future, it is highly expected that this technique clarifies the heat transfer mechanisms for a complex flow, which has been very difficult to investigate using conventional methods. It is hoped that the knowledge acquired using this technique will be contribute to develop technology in heat transfer control, and also to improve reliability in thermal design of various equipment and machinery.

8. References

Abe, H., Kawamura, H. and Matsuo, Y. (2004). Surface Heat-Flux Fluctuations in a Turbulent Channel Flow up to Re_τ = 1020 with Pr = 0.025 and 0.71, *International Journal of Heat and Fluid Flow*, Vol. 25, 404-419.

Bhattacharjee, S., Scheelke, B., and Troutt, T.R. 1986. Modification of Vortex Interactions in a Reattaching Separated Flow, *AIAA Journal*, Vol.24, 623-629.

Durst, F., and Tropea, C. (1981). Turbulent, Backward-Facing Step Flows in Two-Dimensional Ducts and Channels, *Proc. 3rd Int. Symp. on Turbulent Shear Flows*, pp.18.1-18.6, Davis, CA, 1981.

Eaton, J.K. and Johnston, J.P. (1980). Turbulent Flow Reattachment: An Experimental Study of the Flow and Structure behind a Backward-Facing Step. *Rep.*, MD-39, Thermosciences Division, Dept. of Mech. Engng, Stanford University.

Eaton, J.K. and Johnston, J.P. (1981). A Review of on Subsonic Turbulent Flow Reattachment. *AIAA Journal*, Vol.19, No.9, 1093-1100.

Hetsroni, G. and Rozenblit, R. (1994). Heat Transfer to a Liquid-Solid Mixture in a Flume, *International Journal of Multiphase Flow*, Vol.20-4, 671-689, ISSN 03019322

Igarashi, T. (1986). Local Heat Transfer from a Square Prism to an Air Stream, *Int. J. Heat and Mass Transfer*, Vol.29, No.5, 777-784.

Iritani, Y., Kasagi, N. and Hirata, M. (1983). Heat Transfer Mechanism and Associated Turbulent Structure in the Near-Wall Region of a Turbulent Boundary Layer, *4th Symposium on Turbulent Shear Flows*, pp. 17.31-17.36, Karlsruhe, Germany, 1983.9

Iritani, Y., Kasagi, N. and Hirata, M. (1985). Streaky Structure in a Two-Dimensional Turbulent Channel Flow (in Japanese), *Trans. Jpn. Soc. Mech. Eng.*, Vol. 51, No. 470, B, 3092-3101.

Kawamura, T., Tanaka, S., Kumada, M. and Mabuchi, I. (1988). Time and Spatial Unsteady Characteristics of Heat Transfer at the Reattachment Region of a Backward-Facing Step (in Japanese), *Transactions of Japan Society of Mechanical Engineers B*, Vol. 54, No. 504, 1224-1232.

Kawamura, T., Yamamori, M., Mimatsu, J. and Kumada, M. (1994). Three-Dimensional Unsteady Characteristics of Heat Transfer around Reattachment Region of Backward-Facing Step Flow (in Japanese), *Transactions of Japan Society of Mechanical Engineers B*, Vol. 60, No. 576, 2833-2839.

Kiya, M. and Sasaki, K. (1983). Structure of a Turbulent Separation Bubble, *J. Fluid Mech.*, Vol. 137, 83-113.

Kong, H., Choi, H. and Lee, J.S. (2000). Direct Numerical Simulation of Turbulent Thermal Boundary Layers, *Physics of Fluids*, Vol. 12, No. 10, 2555-2568.

Le, H. Moin, P. and Kim, J. (1997). Direct Numerical Simulation of Turbulent Flow Over a Backward-Facing Step. *J. Fluid Mech.*, Vol. 330, 349-374.

Lee, I. and Sung, H.J. (2002). Multiple-Arrayed Pressure Measurement for Investigation of the Unsteady Flow Structure of a Reattaching Shear Layer, *J. Fluid Mech.*, Vol. 463, 377-402.

Lu, D.M. and Hetsroni, G. (1995). Direct Numerical Simulation of a Turbulent Open Channel Flow with Passive Heat Transfer, *Int. J. Heat and Mass Transfer*, Vol. 38, No. 17, 3241-3251.

Nakamaru M, Tsuji M, Kasagi N and Hirata M. (1980). A Study on the Transport Mechanism of Separated Flow behind a Step, 2nd Report (in Japanese), *17th National Heat Transfer Symp. of Japan*, pp.7-9.

Nakamura, H. (2007a). Measurements of time-space distribution of convective heat transfer to air using a thin conductive-film, *Proceedings of 5th International Symposium on Turbulence and Shear Flow Phenomena*, pp. 773-778, München, Germany, 2007.8

Nakamura, H. (2007b). Measurements of Time-Space Distribution of Convective Heat Transfer to Air Using a Thin Conductive Film (in Japanese), *Transactions of Japan Society of Mechanical Engineers B*, Vol. 73, No. 733, 1906-1914.

Nakamura, H. (2009). Frequency response and spatial resolution of a thin foil for heat transfer measurements using infrared thermography. *International Journal of Heat and Mass Transfer,* Vol.52, 5040-5045, ISSN 00179310

Nakamura, H. (2010). Spatio-temporal measurement of convective heat transfer for the separated and reattaching flow, *Proceedings of 14th International Heat Transfer Conference*, IHTC14-22753, Washington, DC, USA, 2010.8.

Oyakawa, K., Miyagi, T., Oshiro, S., Senaha, I., Yaga, M., and Hiwada, M. (2000). Study on Time-Spatial Characteristics of Heat Transfer by Visualization of Infrared Images and Dye Flow, *Proceedings of 9th International Symposium on Flow Visualization*, Pap. no. 233, Edinburgh, Scotland, UK, 2000.

Peaceman, D.W. and Rachford, H.H. (1955). The numerical solution of parabolic and elliptic differential equations, *J. Soc. Ind. Appl. Math.*, Vol.3, 28-41.

Richardson, P.D. (1963). Heat and Mass Transfer in Turbulent Separated Flows, *Chemical Engineering Science*, Vol.18, 149-155.

Schäfer, F., Breuer, M. and Durst, F. (2007). The Dynamics of the Transitional Flow Over a Backward-Facing Step, *J. Fluid Mech.*, Vol. 623, 85-119.

Tiselj, I., Pogrebnyak, E., Li, C., Mosyak, A., and Hetsroni, G. (2001). Effect of Wall Boundary Condition on Scalar Transfer in a Fully Developed Turbulent Flume, *Physics Fluids*, Vol. 13, No. 4, 1028-1039.

Vogel, J.C. and Eaton, J.K. (1985). Combined Heat Transfer and Fluid Dynamic Measurements Downstream of a Backward-Facing Step, *Trans. ASME J. Heat Transfer*, Vol.107, 922-929.

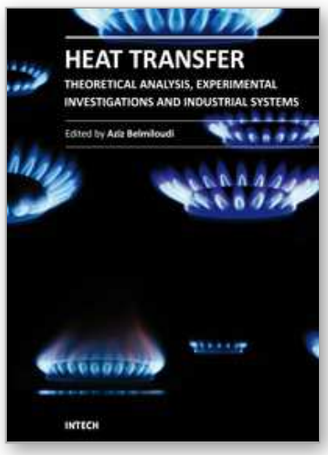

Heat Transfer - Theoretical Analysis, Experimental Investigations and Industrial Systems

Edited by Prof. Aziz Belmiloudi

ISBN 978-953-307-226-5
Hard cover, 654 pages
Publisher InTech
Published online 28, January, 2011
Published in print edition January, 2011

Over the past few decades there has been a prolific increase in research and development in area of heat transfer, heat exchangers and their associated technologies. This book is a collection of current research in the above mentioned areas and discusses experimental, theoretical and calculation approaches and industrial utilizations with modern ideas and methods to study heat transfer for single and multiphase systems. The topics considered include various basic concepts of heat transfer, the fundamental modes of heat transfer (namely conduction, convection and radiation), thermophysical properties, condensation, boiling, freezing, innovative experiments, measurement analysis, theoretical models and simulations, with many real-world problems and important modern applications. The book is divided in four sections : "Heat Transfer in Micro Systems", "Boiling, Freezing and Condensation Heat Transfer", "Heat Transfer and its Assessment", "Heat Transfer Calculations", and each section discusses a wide variety of techniques, methods and applications in accordance with the subjects. The combination of theoretical and experimental investigations with many important practical applications of current interest will make this book of interest to researchers, scientists, engineers and graduate students, who make use of experimental and theoretical investigations, assessment and enhancement techniques in this multidisciplinary field as well as to researchers in mathematical modelling, computer simulations and information sciences, who make use of experimental and theoretical investigations as a means of critical assessment of models and results derived from advanced numerical simulations and improvement of the developed models and numerical methods.

INTECH
open science | open minds

InTech Europe
University Campus STeP Ri
Slavka Krautzeka 83/A

InTech China
Unit 405, Office Block, Hotel Equatorial Shanghai
No.65, Yan An Road (West), Shanghai, 200040, China

51000 Rijeka, Croatia
Phone: +385 (51) 770 447
Fax: +385 (51) 686 166
www.intechopen.com

中国上海市延安西路65号上海国际贵都大饭店办公楼405单元
Phone: +86-21-62489820
Fax: +86-21-62489821

IntechOpen

IntechOpen